

# Forced two-dimensional turbulence in spectral and physical space

Sergey Danilov<sup>1,\*</sup> and David Gurarie<sup>2,†</sup><sup>1</sup>*Institute of Atmospheric Physics, Moscow, Russia*<sup>2</sup>*Case Western Reserve University, Cleveland, Ohio*

(Received 1 August 2000; revised manuscript received 23 February 2001; published 25 May 2001)

Two-dimensional (2D) turbulence in the energy range exhibits nonuniversal features, manifested in the departure (at low  $k$ ) from the  $k^{-5/3}$  energy spectrum law, variable energy flux, and irregular, nonlocal transfers. To unravel the underlying mechanism we conducted a detailed study of the 2D turbulence in spectral and physical space. It revealed complex multiscale organization of vorticity field and dynamic processes, ranging from large-scale meandering jets to strong localized vortices. The latter bear prime responsibility for the nonuniversal behavior of 2D turbulence, and we examined their statistical features and the growth mechanism. Our results are based on the numeric simulation of 2D turbulence on the 512 grid under different forcing-dissipation conditions.

DOI: 10.1103/PhysRevE.63.061208

PACS number(s): 47.10.+g, 05.40.-a, 47.27.-i

## I. INTRODUCTION

The standard KBL (Kraichnan–Batchelor–Leith) phenomenology of 2D incompressible turbulence exploits its two conserved integrals, energy and enstrophy, and predicts two inertial intervals, above and below the forcing scale. The upscale energy flux should give, according to the theory, the  $k^{-5/3}$  energy spectrum, while the downscale enstrophy flux gives the energy spectrum with the slope  $-3$ . Both cascades should be sustained by constant fluxes (dissipation rates) of energy  $\varepsilon$  and enstrophy  $\eta$  through local transfers.

Since its inception the theory went through an extensive numeric and experimental study to verify its premises and predictions. Early works ([1,2]) seem to confirm the  $k^{-5/3}$  spectra in the energy range and later studies found links to some physical space properties: velocity increments and their statistical moments ([3–7]). It was shown, in particular, that the longitudinal velocity has even moments of its increments close to Gaussian, while its third-order structure function obeys the Kolmogorov-type  $3/2$  law.

Though most efforts have so far focused on reproducing universal features, some authors observed strong departures from universality, like spectra deviating from the  $-5/3$  law [8], or nonlocal transfers and fluxes [9].

An obvious obstacle to universality comes at the very setup of the problem—the energy dissipation mechanism at large scales. The natural way to dissipate energy in 2D flows is via bottom friction (linear drag). Since bottom drag affects all scales uniformly, it invalidates the “dissipation-free” inertial interval in the energy range. Indeed, numeric simulations and experiments show consistent drop of the energy flux as  $k \rightarrow 0$  in such flows. To recreate a dissipation-free “inertial interval” (with constant flux), some authors apply linear drag selectively to a few gravest modes of the system [10], or replace linear drag by scale-dependent *hypofriction* [8,11].

While hypofriction could produce an almost constant flux

over a large portion of the energy range, it leads, contrary to expectations, to a drastic departure from the  $-5/3$  law [8,12] (spectral slope close to  $-3$ , reported in [8]). On the contrary, simulations with linear drag could give a nearly perfect  $-5/3$  slope, but their energy flux becomes highly nonuniform [13]. Both tendencies are rooted in the nonlocalness of the inverse cascade.

Sukorianski *et al.* [12] claimed that 2D turbulence in the energy range is highly sensitive to the infrared dissipation, and any attempt to abruptly terminate the inverse cascade could drive the spectrum away from  $k^{-5/3}$ . They show that the ideal  $k^{-5/3}$  spectrum could appear in the dissipation-free interval  $[k_{ls}, k_f]$  under special parametrization of “super-grid” modes  $k < k_{ls}$  that “damp excess energy.” Whether realistic or not, this proposal shows the  $k^{-5/3}$  spectra to be highly exceptional.

So the basic problems in 2D turbulence are (i) whether universal  $k^{-5/3}$  spectra are possible, and if so, under what conditions, (ii) what makes the flow depart from universality, and (iii) how to quantify these departures and link them to the flow dynamics?

Some authors associate nonuniversal spectra with strong vortices, most apparent in the hypofrictional case [8]. So one is naturally led to study the physical space structures of 2D turbulence, beyond the standard velocity increments and moments.

There is no clear picture (consensus) on the physical space structure of turbulence and conflicting claims are often made. Some authors (e.g., [8]) view inverse cascade as the “growth of strong vortices sustained by vortex mergers.” Other works [7,6] argue for “agglomeration” as the principal organizing process but give little detail or explanation. Vortices have been consistently observed in numeric simulations [10] but usually at the forcing (or nearby) scales far from the energy peak. It remains unclear whether such vortices could form spectra of the inverse cascade range and how they would do it.

Our paper aims to address and quantify some nonuniversal features of the inverse cascade and examine the underlying physical space dynamics. To this end we conducted a series of numeric experiments with the 512<sup>2</sup> pseudospectral

\*Present address: NCAR, P.O. Box 3000, Boulder, CO 80307.

†Email address: gurarie@ucar.edu

code in several regimes of linear friction, as well as hypofriction, and frictionless systems. On the spectral side we saw systematic departures from the universal behavior reported in [13] and reviewed here. They take on several forms: (i) spectral bulge in the compensated spectrum  $k^{5/3}E(k)$ , (ii) inconsistency of the  $-5/3$  slope with constant energy flux, and (iii) highly irregular and nonlocal transfers whereby forcing-scale modes couple directly to the energy-peak (infrared) modes.

Our study of the physical space vorticity field revealed two levels of organization: *background* and large-scale secondary flow. The former consists of small (forcing size) vorticity patches, unstable due to straining and filamentation, the velocity field is nearly Gaussian and the energy spectrum remains close to  $k^{-5/3}$ . The secondary structures evolve from the  $k^{-5/3}$  background [8] and could take on two forms: (i) *clusters* of the background patch density along with larger circulation zones and jets, (ii) *strong localized vortices* that develop from the local vorticity extrema, under favorable conditions

We focus our attention on strong vortices, examine their statistical and dynamic features, the role of forcing and friction in the evolution of the system, its statistical equilibration, links between large-scale structures, vortices and energy spectra. Our results corroborate some earlier findings and proposals on the “vortex role” in nonuniversality. But they also reveal some unexpected results, particularly, the statistical mechanisms of vortex growth.

Our results also suggest a possible alternative to the “spectral cascade” phenomenology in physical space: it could be based (at least partly) on the stochastic model of the vortex growth/ dynamics. The complete theory of the physical space turbulence wanting, we mostly describe our observations and attempt to draw some conclusions and outline conceivable mechanisms, as well as formulate problems. We hope the future work will clarify some of these issues.

The paper is organized in four sections. Section II outlines the numeric procedures and experiments, Sec. III describes “nonuniversality” in spectral space, while Sec. IV deals with the physical space structures and processes.

## II. NUMERICAL EXPERIMENTS

We use the standard vorticity formulation of 2D hydrodynamics in terms of stream field  $\psi(\mathbf{x}, t)$  and its vorticity  $\zeta = \Delta\psi$ ,

$$\partial_t \zeta + J(\psi, \zeta) = D\zeta + f. \quad (1)$$

Here  $J(\psi, \zeta) = \partial_x \psi \partial_y \zeta - \partial_y \psi \partial_x \zeta$  denotes the Jacobian of  $\psi$  and  $\zeta$ ,  $f$  represents external (driving) force, and  $D$  is the dissipation operator at low and high wave numbers  $k$ . One normally takes it in the form of “friction + viscosity,”  $D = -\lambda + \nu\Delta$ , or more generally, “hypofriction + hyperviscosity”  $D = -\lambda(-\Delta)^{-m} - \nu(-\Delta)^n$ , implemented via positive/negative powers of the Laplacian.

The Fourier transform of Eq. (1) takes on the form

$$\partial_t \zeta_{\mathbf{k}} + J_{\mathbf{k}} = D_{\mathbf{k}} + f_{\mathbf{k}}, \quad (2)$$

TABLE I. Runs with linear drag.

	$k_f$	$\lambda$	Hyperviscosity	$\varepsilon$ (units of $10^4$ )	Kurtosis	$k_{peak}$
1	100	0.1	$\nu=2; n=2$	6.5	3.5	26
2	100	0.05	$\nu=2; n=2$	6.6	3.5	15
3	100	0.03	$\nu=2; n=2$	6.7	4.5	9
4	100	0.02	$\nu=2; n=2$	6.6	5.5	6
5	100	0.015	$\nu=2; n=2$	6.5	7.0	4
6	100	0.05	$\nu=2; n=2$	25	4.6	9
7	100	0.03	$\nu=2; n=2$	4.4	4.2	9
8	100	0.05	$\nu=2; n=2$	4.4	3.8	21
9	150	0.03	$\nu=20; n=8$	13	3.5	6
10	150	0.02	$\nu=20; n=8$	13	3.9	3
11	150	0.03	$\nu=20; n=8$	20	3.5	6
12	150	0.03	$\nu=20; n=8$	5.1	3.5	9
13	60	0.03	$\nu=2; n=2$	9.6	3.7	6
14	80	0.03	$\nu=20; n=8$	20	3.4	5
15	80	0.03	$\nu=40; n=4$	34	7.3	4
16	80	0.05	$\nu=40; n=4$	34	5.2	9
17	100	0.03	$\nu=20; n=4$	25	5.3	5

for  $\mathbf{k}$ th modes of each term (1), and the dissipation operator becomes diagonalized

$$D_{\mathbf{k}} = - \left[ \lambda \left( \frac{k_0}{k} \right)^{2m} + \nu \left( \frac{k}{k_{max}} \right)^{2n} \right] \zeta_{\mathbf{k}}.$$

The low cutoff wave number  $k_0$  marks the region of high hypofriction, while  $k_{max}$  denotes the maximum resolved wave number. Case  $m=0$  corresponds to the linear drag used in most our experiments.

We integrate system (2) by the fully dealiased pseudospectral method [14]. In this algorithm  $k_{max} = 0.94(N/2)$ , where  $N$  measures the number of grid points along the axis. Most our simulations run at resolution  $N=512$ , with a few exceptions at  $N=256$ . The time stepping was implemented by the third-order Adams-Bashforth method [15].

Following [10] we force the system with a Markovian process:  $f_{\mathbf{k}}(t + \delta t) = A(1 - r^2)^{1/2} e^{i\theta} + r f_{\mathbf{k}}(t)$  ( $t$  marks discrete time steps) of amplitude  $A$ , correlation radius  $\delta t/(1 - r)$ , and random uniformly distributed phases  $\theta$  on  $[0, 2\pi]$ . In most experiments, the source was localized within narrow spectral range  $(k_f - 2, k_f + 2)$  in the vicinity of the forcing wave number  $k_f$ . Time step  $\delta t$  in experiments with linear drag was 0.002. It was reduced to 0.001 in the frictionless or hypofriction experiments.

Table I records the basic input parameters along with the vorticity kurtosis and the energy peak wave number in the linear drag cases, while Table II does it for the hypofriction, and frictionless runs.

Runs 13 and 14 were performed at lower resolution  $N=256$ . Time correlation parameter was chosen as  $r=0.9$  in runs 1–6, 13, 17 and 4h, and  $r=0.5$  in all other runs. Besides runs 11 and 12 had a wider range of the forcing wave numbers  $(k_f - 5, k_f + 5)$ . In all linear-drag cases we integrated the system for several (up to 9) units of the friction dissipation time  $1/\lambda$ , to ensure the energy and enstrophy stabilization.

TABLE II. Runs with hypofriction and without friction

	$k_f$	Friction	Hyperviscosity	$\varepsilon$ (units of $10^4$ )	Kurtosis	$k_{peak}$
1h	100	$0.01(10/k)^4$	$\nu=2; n=2$	3.0	39	12
2h	80	$0.03(8/k)^4$	$\nu=40; n=4$	36	38.8	10
3h	80	$0.03(6/k)^4$	$\nu=20; n=8$	20	27	8
4h	100	$0.03(8/k)^4$	$\nu=20; n=4$	25	31	9
1n	150	no	$\nu=3.5; n=2$	1		
2n	100	no	$\nu=3.5; n=2$	2.5		
3n	100	no	$\nu=50; n=8$	2.5		

The frictionless cases 1n–3n could run only for a limited time span due to the energy accumulation in the lowest modes, typically up to 50 computational time units,<sup>1</sup> that suffices for the energy equilibration in most linear-drag cases.

The energy peak wave number  $k_p$  marks the arrest scale of the inverse cascade.

### III. NONUNIVERSAL FEATURES OF INVERSE CASCADE

#### A. Energy spectra and fluxes

Figure 1 shows compensated energy spectra  $k^{5/3}E(k)$ , and energy fluxes

$$\Pi(k) = - \sum_{k' \leq k} T_{k'}, \quad T_{\mathbf{k}} = \text{Re}(\psi_{-\mathbf{k}} J_{\mathbf{k}})$$

obtained in experiments 1–5. Here  $T_{\mathbf{k}}$  are transfers into the mode  $\mathbf{k}$ . The energy fluxes are variable and the energy dissipation rate is connected to them by  $\varepsilon = \max|\Pi(k)|$ . In series 1–5 we fixed forcing and let the drag coefficient  $\lambda$  vary. Formally, linear drag should equilibrate the total energy on time scale  $1/2\lambda$ , a consequence of the (approximate) balance

$$(\partial_t + 2\lambda)E_{tot} \approx \varepsilon.$$

Indeed, in our experiments the total energy has negligible fluctuations at later times ( $t > 3/\lambda$ ), but its isotropic spectra  $E(k)$  still fluctuate noticeably. Thus spectra of Fig. 1(a) obtained after long averaging (several times  $1/\lambda$ ) would keep oscillating in the infrared region.

Notice, that compensated spectra contain the plateau interval near the source, but it does not imply the constant energy flux. Indeed, in the linear-drag case we observe the tendency of flux  $\Pi$  to drop down to zero as  $k \rightarrow 0$ , faster than any noticeable change would occur in the spectral slope that is well within the plateau region, consistent with the results of [7,6].

Another important observation has to do with the opposite trends of the energy spectra and fluxes as one changes fric-

tion coefficient  $\lambda$ . Decreasing  $\lambda$ , the energy flux becomes more uniform, while compensated spectra develop a more pronounced bulge at the low end. That clearly violates the idea of locality, as “local cascade” would imply simultaneous increase or decrease of  $E(k)$  and  $\Pi(k)$ , while we see the opposite trends over a broad range of  $\lambda$ .

As a consequence, the Kolmogorov constant  $C_K$ , defined by local values of the energy density and flux, becomes a function of  $k$  [thin lines of Fig. 1(a), computed in runs 1 and 5]. Its mean value, close to 6, agrees with some recent estimates [10,6,7]. But the wide scatter of  $C_K$  reported in the literature could be attributed to an attempt to represent the variable quantity  $C_K$  by a single value.

While mean flux shows an apparent decay trend, one might wonder whether a proper account of its fluctuations, raised to the power  $2/3$  (in the  $-5/3$  law) would make it more uniform (consistent with phenomenology) over the plateau region. It turns out that the flux variance is always mod-

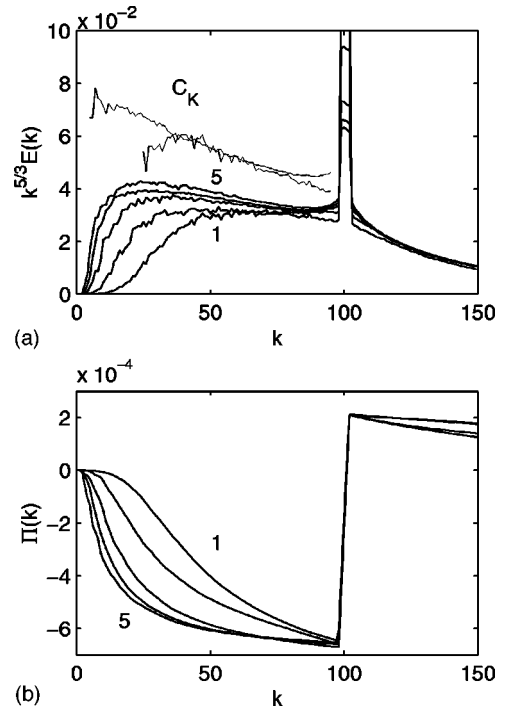


FIG. 1. Compensated energy spectra (a) and energy fluxes (b) in experiments 1–5. Thin solid lines in (a) are the Kolmogorov constants for experiments 1 and 5. Curves labeled with 1 and 5 correspond to experiments 1 and 5, respectively.

<sup>1</sup>The computational time unit are nondimensionalized by multiplying them with  $\eta^{1/3} = (\varepsilon k_f^2)^{1/3} \approx 1.3$ —enstrophy at the forcing scale. So they characterize the vortex-turnover time on the forcing scale.

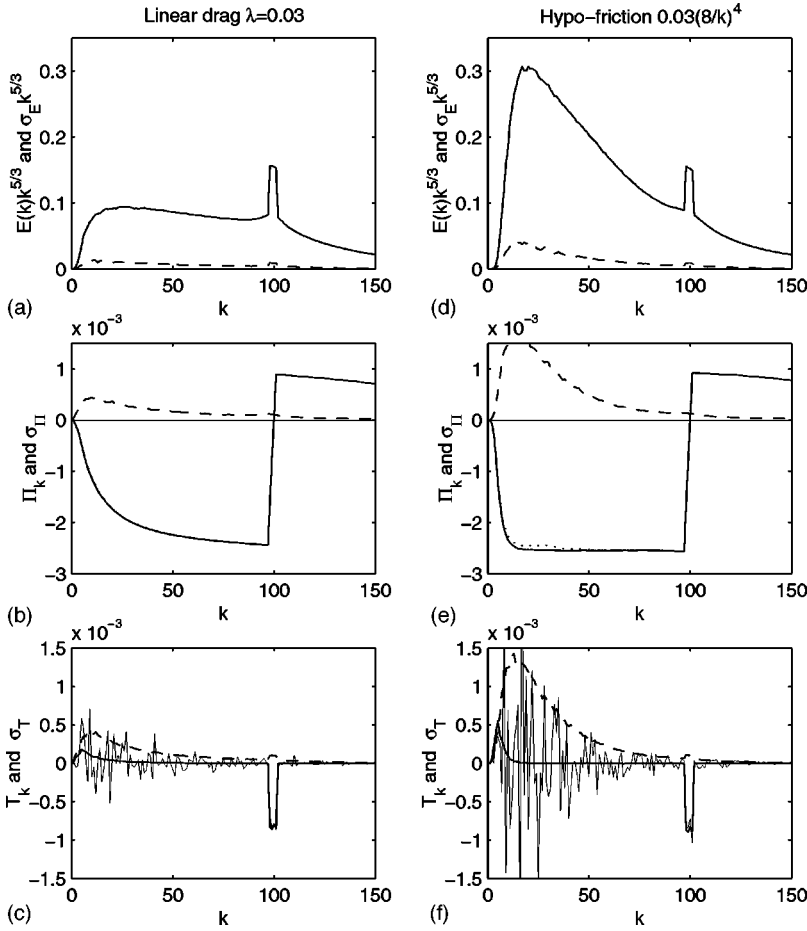


FIG. 2. Compensated energy spectra (a), (d), energy spectral fluxes (b), (e) and energy transfers (c), (f), and their variances (dashed) in experiments 17 (a), (b), (c) and 4h (d), (e), (f). The dotted lines in (b) (hardly seen) and (e) show  $\Pi_{2/3}(k)$

erate for linear-drag simulations, so it will not affect our main conclusion. Indeed, Figs. 2(a) and 2(b) present energy and flux along with their variances  $\sigma_E$  and  $\sigma_{\Pi}$  for experiment 17 whose energy production rate was four times the rate of experiments 1–5. Variances are defined in the usual way,  $\sigma_E^2(k) = (M-1)^{-1} \sum_{n=1}^M [E(k, t_n) - E(k)]^2$  for energy and a similar form for flux. The averaging period was taken as  $3/\lambda$  and averaging was performed over approximately  $M = 1000$  realizations. The dotted line in Fig. 2(b) shows the time average of  $\Pi(k, t)^{2/3}$  raised to the power  $3/2$  and multiplied with  $\text{sgn } \Pi(k)$ . It will be further denoted as  $\Pi_{2/3}(k)$ . The difference between  $\Pi_{2/3}(k)$  and the mean flux  $\Pi(k)$  is hardly noticeable.

Let us remark that similar divergent trends between the energy spectrum and flux appear in other experiments and regimes, including the eddy-damped quasinormal Markovian (EDQNM) simulations [13]. They all confirm our main conclusion that the nearly perfect  $k^{-5/3}$  spectrum is typically accompanied by nonuniform flux  $\Pi(k)$ , and any attempt to produce constant  $\Pi(k)$  would result in spectral bulge. Similar conclusions could also be drawn from the recent high-resolution simulations of [7] (Fig. 2 therein). The laboratory experiment of [6] (Figs. 2 and 3 therein) shows yet larger departure, with  $-5/3$  slope stretching far into the region where the flux becomes negligible.

The nonlocality of transfers becomes most apparent in simulations with hypofriction. Figures 2(d) and 2(e) present the energy spectrum and flux for experiment 4h (thin lines),

similar to experiment 17 in other parameters except for hypofrictional dissipation. It shows almost uniform flux over the large fraction of the energy interval, while its spectrum departs dramatically from the  $-5/3$  law. The actual slope has no single exponent, it comes close to  $-3$  over an octave near the forcing range, and grows shallower at the lower end. Once again we see nonlocal energy transfers. Variances of the energy spectrum and flux in hypofriction case increase, see Figs. 2(d) and 2(e), but remain moderate for the most part of the energy interval. The energy flux shows stronger fluctuations than the energy spectrum, and its variance  $\sigma_{\Pi}$  could attain values comparable to the flux itself at the peak region. One could also observe that  $\Pi_{2/3}(k)$  [Fig. 2(e), dotted line] deviates from mean flux, but this deviation is positive and cannot account for departure from the  $-5/3$  law. So flux fluctuations seem to play a minor role in the hypofrictional case as well.

In all cases the formation of spectral bulge is accompanied by a strong deviation of the vorticity kurtosis

$$Ku = \langle \zeta(x, y)^4 \rangle / \langle \zeta(x, y)^2 \rangle^2$$

from its Gaussian value 3. Here angular brackets denote area averaging. Kurtosis remains virtually constant after turbulence reaches the stationary regime. In experiments 1–5  $Ku$  varied between 3.5 and 7, as  $\lambda$  varied from 0.1 to 0.015. Such deviations, though moderate, indicate the presence of vortices in physical space.



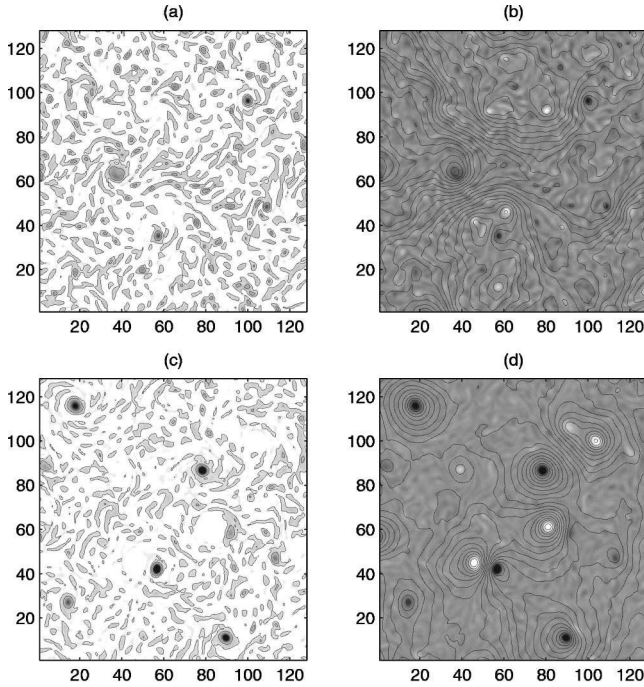


FIG. 3. Fragments of vorticity field ( $128 \times 128$  grid points) from runs 17 (a), (b) and 4h (c), (d). In (a) and (c) only negative vorticity is shown. Contours are drawn for  $|\zeta| = (0.5, 2)\zeta_{rms}$ . In (b) and (d) white areas correspond to positive, and black to negative vorticity. The contours are drawn for stream function.

In Sec. IV we shall address properties of vortices in more detail. But here we shall illustrate the vorticity pattern for experiments 17 [Figs. 3(a) and 3(b)] and 4h [Figs. 3(c) and 3(d)]. The size of vorticity patches on forcing scale  $L_f = \pi/k_f$  is approximately 2.5 grid intervals. The vorticity kurtosis in experiment 17 takes on a moderate value 5.3, and vortex population (see figure caption for explanation) gives minor contribution to the velocity field as evidenced by the streamline pattern of Fig. 3(b). The energy spectrum remains close to the  $-5/3$  law [Fig. 2(a)]. Vortices grow much stronger in hypofriction experiments and start dominating the velocity field [cf. Figs. 3(c) and 3(d)]. Concurrently, we observe the energy spectrum deviating strongly from  $k^{-5/3}$  [Fig. 2(d)].

The magnitude of the bulge depends on  $\varepsilon, \lambda$ , as well as the dynamics of the forcing range, and the spectral width of the energy and enstrophy intervals. Thus bulges observed in experiments 9 and 10 are less pronounced, compared to those of 3 and 4, despite increased  $\varepsilon$  (by factor 2). Lower kurtosis in experiments 9 and 10, compared to experiments 3 and 4, also indicates less intense vortices. We attribute it to a poor resolution of the enstrophy range, whereby strong hyperviscosity efficiently dissipates long filaments and small-scale structures conducive to the large-scale organization.

While our experiments do not allow more definite conclusions regarding enstrophy resolution (or other forcing scale processes), they clearly relate the appearance of bulge to vortices. Damping vorticity production at the forcing range, (by hyperviscosity) would typically flatten spectra and bring them close to  $k^{-5/3}$ . Borue [8] noticed such sensitivity and

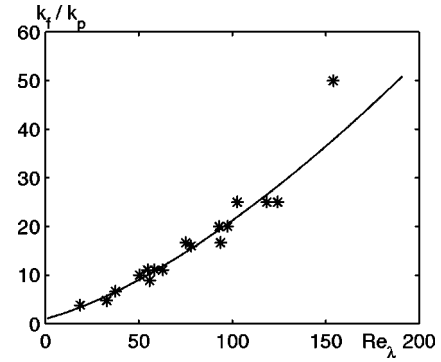


FIG. 4. Ratio  $k_f/k_p$  as a function of friction Reynolds number: experiments 1–17\*, solid line corresponds to Eq. (3) with  $C_K = 5$ .

argued that strong vortices would form only if both ultraviolet (hyperviscosity) and infrared (friction) Reynolds numbers are sufficiently high.

Thus a proper choice of forcing-dissipation parameters could practically eliminate spectral bulge in the linear-drag case (not in other cases), but that comes at the expense of nonuniform energy flux due to nonlocality.

One of the basic problems in the inverse cascade is the proper parametrization of the energy-peak scale  $k_p$ . The standard approach, going back to Lilly [16], looks for an estimate in terms of  $\lambda$  and the energy dissipation rate  $\varepsilon = \max|\Pi(k)|$ . In the linear-drag case one could derive such an estimate, assuming the standard energy spectrum  $k^{-5/3}$  between  $k_p$  and  $k_f$ , hence total energy  $E \approx \int_{k_p}^{k_f} C_K \varepsilon^{2/3} k^{-5/3} dk$  and  $2\lambda E \approx \varepsilon$ . Then one gets

$$\frac{k_p}{k_f} \approx [1 + (3C_K)^{-1} \text{Re}_\lambda]^{-3/2} \quad (3)$$

where

$$\text{Re}_\lambda = (\varepsilon k_f^2)^{1/3} / \lambda$$

is the friction Reynolds number. If  $\text{Re}_\lambda / (3C_K)$  is large, the dependence on  $k_f$  drops down and the estimate for  $k_p$  becomes

$$k_p \approx (3C_K)^{3/2} \left( \frac{\lambda^3}{\varepsilon} \right)^{1/2}. \quad (4)$$

When compared to our experimental data, estimate (3) shows good qualitative agreement, see Fig. 4.

A similar estimate, with slightly different coefficients, could be derived from a simple closure scheme for the energy equation,

$$(\partial_t + 2\lambda)E_k = T_k + \varepsilon \delta(k - k_f). \quad (5)$$

We express the transfer term  $T_k = -\partial_k(k\mu_k E_k)$  through the “relaxation rate” of large eddies,  $\mu_k = a(\int_0^k p^2 E_p)^{1/2}$ , with an undetermined coefficient  $a$ . Assuming linear friction law (constant  $\lambda$ ), Eq. (5) allows an analytic solution for  $E_k$  that yields an estimate

$$\frac{k_p}{k_f} \approx .85 \left[ 1 + \left( \frac{3a^2}{2} \right)^{1/3} \text{Re}_\lambda \right]^{-3/2}.$$

The latter agrees with our data for  $a \approx .01$ .

### B. Nonlocal transfers

We recall the spectral energy equation

$$(\partial_t - 2D_k)E(k) = \sum_{|\mathbf{k}|=k} (f_{\mathbf{k}} + T_{\mathbf{k}}),$$

where

$$T_{\mathbf{k}} = \text{Re}(\psi_{-\mathbf{k}} J_{\mathbf{k}}) = \sum_{\mathbf{p}+\mathbf{q}=\mathbf{k}} A_{\mathbf{pq}}^{\mathbf{k}} \text{Re}(\zeta_{\mathbf{p}} \zeta_{\mathbf{q}} \zeta_{\mathbf{k}}^*)$$

and

$$A_{\mathbf{pq}}^{\mathbf{k}} = \mathbf{p} \times \mathbf{q} \left( \frac{1}{\mathbf{p}^2} - \frac{1}{\mathbf{q}^2} \right)$$

are (Jacobian) structure coefficients. We expand the  $\mathbf{k}$ th transfer term  $T_{\mathbf{k}}$  into the sum of partial transfers  $T_{\mathbf{k},\mathbf{p}}$ , that represent contributions of various pairs  $\{\mathbf{p}, \mathbf{q}\}$  to the  $\mathbf{k}$ th mode (cf. [9]). The isotropic transfers  $T_k$ ,  $T_{kp}$  are obtained by summing over all equal length wave vectors,  $|\mathbf{k}| = k$ ,  $|\mathbf{p}| = p$ .

Isotropic transfers  $T_k$  have highly irregular realizations and more so partial transfers. In Figs. 2(c) and 2(f) we present realizations of transfers, mean transfers, and transfer variances from runs 17 and 4h. Contrary to the mean energy spectrum and mean flux, the mean transfer departs strongly from its realizations due to high variance. One would expect it in the inertial interval where the mean transfer is almost zero. We observe it, however even in the energy peak region. The transfer variance is largest there, and based on observations, we could associate it with long-lived fluctuations.

Maltrud and Vallis [9] observed that  $T_k$  combine local and nonlocal contributions, and the nonlocal ones are largely responsible for the inverse cascade. Indeed, the bulk of energy according to [9] is carried over by elongated triads with two long legs  $\{p, q\}$  in the forcing/enstrophy intervals.

We examined energy transfers in experiment 14 with linear drag and experiment 3h with hypofriction. Both experiments had lower resolution  $N=256$ , because computations of averaged partial transfers (for over  $t=2/\lambda$  in experiment 14 and the same in 3h) become prohibitively slow at higher resolution. We also measured transfers in experiment 11 at a resolution of 512, averaging it over shorter time intervals. We observed the same behavior as in the lower-resolution experiment although the measured transfers were less regular.

Figure 5 shows resolved transfers  $T_{kp}$  in experiments 14 and 3h, for wave numbers  $k=10$  (a), 30 (b), 50 (c), and 80 (d). Solid lines correspond to experiment 14 and thin lines to experiment 3h. Transfers are highly irregular at small  $k$  and remain so after long averaging. The energy spectrum in ex-

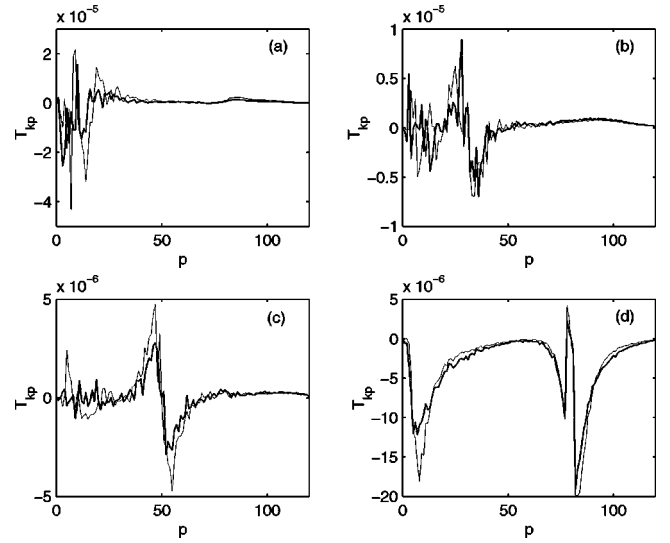


FIG. 5. Energy transfers  $T_{kp}$  in experiments 14 (solid lines) and 3h (thin lines): (a)  $k=10$ , (b)  $k=30$ , (c)  $k=50$ , and (d)  $k=80$ .

periment 14 is very close to  $k^{-5/3}$ , and it is much steeper (with a slope of  $-2.5$  over a narrow interval close to  $k_f$ ) in experiment 3h.

On the whole, our numerics confirmed [9]. Namely, for  $k$  between the energy peak ( $k_p=3-10$ ) and forcing scale [Figs. 5(b) and 5(c)], the principal contribution to  $T_k$  comes from triads with  $p$  in the vicinity of  $k$ . Besides, the  $k$  modes would gain energy ( $T_{kp}>0$ ) from triads with  $p<k, p \approx k$ , and lose it to  $p>k, p \approx k$ . So the (local) energy transport near  $k$  proceeds primarily in the downscale (forward) direction. The inverse transfer to  $k$  involves triads with  $p$  in the forcing (or enstrophy) range, hence is highly nonlocal (large  $p$  would require large  $q$  to form a triad with a small  $k$ ). For  $k$  at the energy peak [Fig. 5(a)] positive contribution comes mostly from  $p$  on the right of  $k_p$  and to a lesser degree from nonlocal triads ( $p$ —in the forcing range). The wave numbers  $k$  in the forcing range [Fig. 5(d)] lose considerable portion of their energy to small  $p$  at the energy peak. Let us also remark that transfers of experiments 14 and 3h look similar, despite substantial differences in the energy spectra and the vorticity field (the differences are similar to those shown in Figs. 2 and 3).

To summarize we find spectral transfers to be highly nonlocal and irregular in space and time. This indicates unstable, transient, and irregular physical space structures responsible for the transfer. We shall discuss them in Sec. IV.

### C. Nonstationary turbulence

Smith and Yakhot [3] studied frictionless (hence nonstationary) 2D turbulence, and observed the  $k^{-5/3}$  spectra and near Gaussian velocities at the initial stage, before the energy peak has reached the box size. Their simulations, however, completely suppressed the enstrophy interval by hyperviscosity. When hyperviscosity was lowered, they saw much steeper spectra at the initial phase (slope  $-2.2$  in Fig. 14 of [3]) and the concurrent formation of vortices. Thus nonuni-

versality could appear right at the start of the turbulent evolution and is evidently linked to the small scales processes in the enstrophy range.

In our frictionless experiments, only spectra of 1n remained close to  $k^{-5/3}$  initially as the vortex production was strongly suppressed at the forcing scale. Spectra of experiment 2n developed substantial spectral bulge accompanied by strong vortices during turbulence evolution. Spectra of experiment 3n deviated from  $k^{-5/3}$  from the start. The spectral slope varied during its evolution reaching values ( $-2.2$  to  $-2.5$ ) by the end of simulation. Robust vortices grew in size and intensity.

We find once again the universal  $k^{-5/3}$  spectrum to be highly exceptional and unstable even at the early (nonstationary) phase. The above deviations from  $k^{-5/3}$  are associated with vortices. We also find [3] that strong damping at the forcing/enstrophy scale could inhibit their formation and hence temporarily recreate a universal behavior. But the subtle dependence of the “large scale spectra” on “enstrophy resolution” signifies nonlocality of the inverse cascade.

In our search of an explanation we turn next to the physical space description.

#### IV. PHYSICAL SPACE TURBULENCE

The physical space 2D turbulence follows a complex multiscale evolution, but we could roughly distinguish two stages along with the associated time scales: (i) enstrophy saturation on time scale  $\tau_\Omega$ , (ii) energy saturation on time scale  $\tau_E$ .

The two scales are well separated,  $\tau_\Omega \ll \tau_E$ , with a fast enstrophy process followed by the slow energy one.

We get a rough estimate of  $\tau_\Omega$  in terms of the enstrophy production rate  $\eta = \varepsilon k_f^2$  and dissipation scale  $k_d \sim k_{\max}(\eta^{1/3}/\nu)^{1/2n} < k_{\max}$  (for hyperviscosity of order  $2n$ ). Under these assumptions and the conventional enstrophy range spectrum  $E(k) = C\eta^{2/3}k^{-3}$ , we get<sup>2</sup>

$$\tau_\Omega \sim \eta^{-1/3} \ln(k_d/k_f).$$

In a similar vein we could estimate the total enstrophy:  $\Omega_0 \approx C\eta^{2/3} \ln(k_d/k_f)$  and the rms vorticity  $\zeta_{rms} = \sqrt{\Omega_0}$  expressed through the same variables,  $\eta$ ,  $k_f$ ,  $k_d$ .

We tracked the initial phase in experiments 15 and 16 and estimated the enstrophy equilibration time at several units  $2\pi/\zeta_{rms}$ . As expected, both  $\tau_\Omega$  and the stationary rms vorticity  $\zeta_{rms} \approx 9.7$  were insensitive to changing  $\lambda$ , while other parameters were held fixed.

The first stage creates a quasistationary *background* field, made of small patches of vorticity about forcing scale in a highly agitated state of production, straining, and dissipation. The slow energy-saturation process leads to formation of secondary structures and (depending on the details of large-

and small-scale dissipation) it could go in two directions: transient large-scale *clusters*, *circulation zones*, and *jets* on the one hand and strong localized *vortices* on the other.

Following [8] we define strong vortices as patches of vorticity above 2 rms ( $|\zeta| > 2\zeta_{rms}$ ), centered at local extrema. In addition we require the mean vorticity over the vortex area to exceed  $2.5\zeta_{rms}$ . In most cases, our selection picks well-identified vortex structures.

Any partition of  $\zeta$  into “background” and “strong vortices” is somewhat arbitrary as in reality one observes a broad spectrum of localized vortex patches, ranging in size, intensity, and shape from small elongated filaments to large vortex cores. Numerous segmentation criteria of vorticity were proposed in the literature (e.g., [17–23]). Some of them (Okubo-Weiss [20,21] or later modifications [23]) focus on topology/geometry of velocity field (elliptic/hyperbolic regions), which would be appropriate for analysis of stirring in 2D turbulent flows, or decaying turbulence. Here we employ a simple Borue-type criterion appropriate for strong localized vortices.

In a typical realization, strong vortices occupy a small area (less than 5%) but carry the bulk of enstrophy, and differ markedly from large, organized vortices of the decaying turbulence [17–19]. Indeed, forced turbulence constrains their size to two to three times the forcing scale but allows high intensity buildup, to 10–15 rms.

Vortices appear in all regimes but in the linear friction case, they have limited size, relatively short life-span, and do not contribute significantly to the energy spectrum (Fig. 2). On the contrary, hypofriction or frictionless turbulence allows strong, well-identified vortices to dominate the dynamics and become principal contributors to the spectrum.

In this section we attempt to quantify some details of vortex dynamics and growth mechanism and the role of forcing dissipation.

##### A. Large-scale organization

The largest-scale organization appears in the form of broad circulation zones and jets. They are clearly visible in the stream field patterns, Fig. 3(b), that show streamlines superimposed on the vorticity field for a particular realization of experiment 17. Averaged energy spectrum in this simulation has a wide plateau with a slope close to the  $-5/3$  slope [Fig. 2(a)] and low  $k_p = 5$ . Circulation zones in physical space enclose clusters of vorticity of variable sign but overall nonzero mean.

The main contribution to the energy peak comes from strong jets on the periphery of the opposing circulation zones. Clearly, mean vorticity on the largest scale is small compared to  $\zeta_{rms}$ , but the very size of zones makes them fairly stable to fast, small-scale processes like patch straining and recombination of vortex clusters. Those tend to redistribute vorticity within zones and deform their periphery, while the mean circulation persists. We measured the decorrelation time of large circulation zones and found it to be  $\tau_{dec} \approx 1/(3\lambda) - 1/(5\lambda)$ , in terms of frictional dissipation time.

Jets persist on yet longer time scale than  $\tau_{dec}$ . This seems to suggest that friction could arrest the inverse energy cas-

<sup>2</sup>Such a relation should hold for sufficient scale separation of  $k_f$  and  $k_d$ , but in most our simulations the enstrophy range was poorly resolved ( $k_f/k_{\max} \sim 1$ ), so  $\tau_\Omega$  should depend on  $k_f/k_{\max}$  rather than  $k_d/k_f$ .



cade, and stabilize the flow on the level of circulating jets. However, the standard explanation of the arrest mechanism of inverse cascade at friction scale,  $L_\lambda$ , appeals to hypothetical “large eddies” whose turnover periods are estimated by  $(L_\lambda^2/\varepsilon)^{1/3}$ . Equating the latter to the friction time  $1/\lambda$ , one gets an estimate:  $L_\lambda \approx C(\varepsilon/\lambda^3)^{1/2}$ , which is consistent with scaling (4). In our experiments we saw no comparable “eddies” and even the largest organized structures (zones and jets) would typically decorrelate over a fraction of  $1/\lambda$ . So “large eddies” would deform and disintegrate faster than “dissipate” and the mechanism of “frictional stabilization” in physical space remains unclear.

### B. Vortices

Localized vortices appear in all regimes of the forced 2D turbulence. Yet under favorable conditions they could grow strong and dominate the dynamics and spectra. Vortex patches and filaments vigorously strain each other and dissipate on forcing scale, so local vorticity extrema could grow into strong vortices if they pass a suitable stability test. Its simplest version (for uniform elliptic vortex patches [21,24]) takes the form

$$s = \zeta_{rms} \leq 0.15 |\zeta_V| \quad (6)$$

in terms of rms strain  $s$  (that coincides with rms vorticity) and mean vorticity  $\zeta_V$  at the vortex core. Sufficiently high  $\zeta_V$  could in principle ensure the vortex survival.<sup>3</sup>

In our linear-drag experiments, the mean vorticity of strongest vortices did not exceed  $(3-4)\zeta_{rms}$  (even for large-kurtosis: experiments 5 and 15), while their extrema were capped below  $10\zeta_{rms}$ , and vortex radii seldom grew above  $(1-1.5)L_f$ . Much stronger and somewhat larger vortices  $[(2-3)L_f]$  evolve in the hypofriction and no-friction systems.

A strong vortex creates a domain of influence (circulation zone) that depends on its intensity  $I$  (vorticity integrated over the 2rms area) and the background. One could estimate the radius of influence by comparing rms velocity  $U_{rms} = \sqrt{2E}$  (of the background field) to the vortex-induced velocity  $V(r) \approx I/r$ , which gives  $R \approx I/U_{rms}$ .

In our experiments (5 and 15) with strong vortices, the radius of influence was roughly 2 vortex radii. Hence vortices could directly contribute to the energy spectrum in the range  $[k_f/6, k_f]$ . Notice, that the low end of this interval extends well within spectral bulge [13]. So we get a clear evidence of the vortex contribution to the bulge.

We get further confirmation by removing all local vorticity protrusions in excess of  $2\zeta_{rms}$ . The resulting “background” field comes very close to the  $k^{-5/3}$  spectrum with only small remnant of the bulge.

To understand vortex contribution to the energy spectrum, we turn next to vortex organization and dynamics.

### 1. Vortex distribution and spectra

To estimate the contribution of vortices to the energy spectra, Benzi *et al.* [18] (cf. [25]) proposed a similarity theory. They consider all vortices to be radially symmetric, and postulate a universal shape function  $Z(r)$  for the vorticity distribution within vortex core. All vortices are then labeled by a single parameter, vortex radius  $R \rightarrow \zeta_R(r)$ , and assumed to be similar to  $Z(r)$  subject to two scaling laws

(i) Self-similarity:  $\zeta_R(r) = R^\alpha Z(r/R)$ , for any radius  $R$

(ii) Vortex distribution by size: number  $n_R$  of vortices of radius  $R$  scales as  $\approx R^{-B}$ . Besides Benzi *et al.* make an additional assumption as follows.

(iii) Vortex positions decorrelate over large time. So after sufficiently long averaging, vortices should occupy all parts of the physical space with equal probability, independent each of the other.

Based on assumptions (i)–(iii) Benzi *et al.* deduced the mean energy spectra of such vortex arrays to be

$$E_k \approx C k^{-6+\beta-2\alpha}$$

where constant  $C$  depends on function  $Z$ . They claimed to verify all three assumptions for the decaying turbulence.

Borue [8] applied their similarity theory to the hypofrictional turbulence. He estimated two critical exponents to be  $\alpha \approx 1/2, \beta = 4$ , and hence got the energy spectral slope,  $E(k) \sim k^{-3}$ , measured in his simulations of the developed turbulent state.

We attempted to reproduce these results in our (lower resolution) hypofrictional experiments. Though our spectral slopes came close to  $-3$ , we could not corroborate the other findings. Namely, the distribution of vortex radii is too narrow:  $R_{\max}/R_{\min} \approx 2-3$  for a reliable statistical inference (Borue had a wider but still limited range  $\approx 5$ ); the measured exponent  $\alpha$  was close to 1 as opposed to  $1/2$  of [8]; we found a tendency of strong vortices to group in vortex dipoles and spend certain time in such bound states, which puts in doubt the “decorrelation hypothesis” (iii).

Overall hypofrictional vortices grow stronger compared to the linear-drag case, as seen by their kurtosis (30–40 vs 5–7). The mean vorticity level of the strongest vortices could reach  $(5-7)\zeta_{rms}$ , while their vortex extrema soar to  $15\zeta_{rms}$  and higher. Yet vortex radii still remain tight,<sup>4</sup> about  $(2-3)L_f$ . Robust vortices in our hypofrictional experiments were approximately Gaussian but we did not pursue their detailed analysis.

Though similar in appearance and scale, the hypofrictional vortices have different effects on the large-scale organization of vorticity compared to the linear-drag case. In Figs. 3(c) and 3(d) we presented a fragment of vorticity field from experiment 4h that includes several dipole features. The background looks faint compared to the linear-drag case [Fig. 3(a)] due to a high core level (above rms). In Fig. 3(d)

<sup>3</sup>Estimates like Eq. (6), based on a simple model of elliptic patch in strain field  $s$ , should not be taken literally but only as a rough cutoff between strong stable vortices and other (transient) extrema of background vorticity.

<sup>4</sup>Borue [8] claimed to produce larger size vortices (up to  $5L_f$ ) with steeper hypofrictional law.



we see streamlines and, consequently energy concentrated around vortex core rather than encircling wide zones as in Fig. 3(b).

Quasistationary forced turbulence involves a balance of source, transfer, and viscous/frictional dissipation. It also sets in a quasistationary vortex distribution. To this end we conducted two sets of experiments, (i) traced the growth-decay dynamics of individual vortices and the principal contributing factors; (ii) focused on the statistical and stochastic features of vortex dynamics.

## 2. Vortex growth

Here we describe the growth dynamics of individual vortices in different regimes, as manifested by a single quantity—vortex intensity and its long term tendencies. We pick a particular positive local extremum above 2 rms, take its local (smoothed) contour area  $A = \{\mathbf{x}: \zeta(\mathbf{x}) \geq 2\zeta_{rms}\}$  and define intensity

$$I_V = \int_A \zeta(\mathbf{x}) dA.$$

The intensity evolution,  $dI_V/dt = D_V + F_V + T_V$ , has three principal sources

$$D_V = \int_A D \zeta dA - (\text{dissipation}), \quad (7)$$

$$F_V = \int_A D \zeta dA - (\text{force}), \quad (8)$$

$$T_V = - \int_A J(\psi, \zeta) dA + \oint_{\Gamma} \mathbf{u} \cdot \nabla \zeta + \dots - (\text{transfer}). \quad (9)$$

The latter, called transfer (or residual) by analogy with the corresponding spectral term, includes the Jacobian, transport across (moving) boundary  $\Gamma$ , and other contributions due to nonconservation of the boundary.

We are interested in the long range integrated tendencies of three factors in the overall balance of  $I_V$ ,

$$D(t) = \int_0^t D_V dt, \quad \mathcal{F}(t) = \int_0^t F_V dt, \quad \mathcal{T}(t) = \int_0^t T_V dt.$$

We conducted a series of experiments in the different regimes of forcing dissipation and found some unexpected results. They reveal a subtle balance between three tendencies of the vortex growth process.

Figure 6(a) shows vortex intensity  $I = I_V$  (1) along with three basic tendencies: forcing  $\mathcal{F}$  (2), dissipation  $\mathcal{D}$  (3), and residual  $\mathcal{T} = I_V - I_V(0) - \mathcal{D} - \mathcal{F}$  in the linear-drag experiment 15. Sharp increases of the vortex intensity (curve 1) result from big mergers. These events are rare in the linear-drag case and we have chosen this particular example to illustrate their presence. Mergers lead to jumps of the vortex intensity due to the increased area. But such increases do not persist, as merged vortex would rapidly shed off the excess (low level) flanks to bring itself to a stable (near circular) configu-

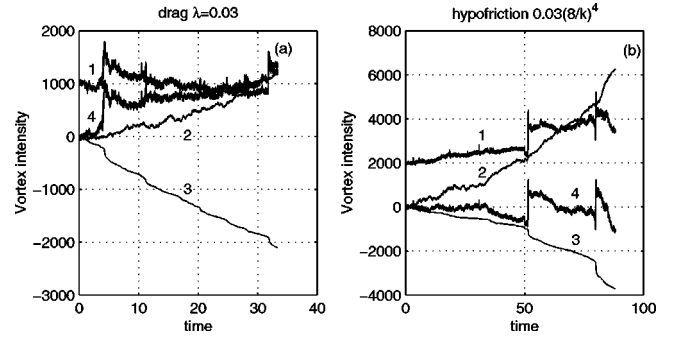


FIG. 6. The tendencies for strong vortices seen in experiment 15 (a) and 2h (b). (1), vortex intensity; (2), forcing tendency; (3), dissipation tendency; (4), residual tendency.

ration. In most cases, the intensity would eventually relax to a premerged state (shown in curve 1), and only rarely would mergers yield a substantial gain. Overall vortex intensity in the linear-drag case fluctuates around some stable level or slowly decays.

A consistent positive trend of the forcing tendency  $\mathcal{F}$  (curve 2—typical of all vortices) looks most puzzling. Indeed, the integrated input of the stochastic source in any fixed area should be zero in the long run. So accumulation could come only through the vortex motion and its “ability” to track the source tendency.

We observed the positive  $\mathcal{F}$  trend (negative for negative vortices) in all regimes and experiments. Furthermore, the cumulative  $\mathcal{F}$  trend was much stronger than the typical residual term  $\mathcal{T}$  (curve 4). The latter could give significant input only through mergers, like in Fig. 6(a), but remains nearly constant otherwise, and close to zero in the absence of mergers.

The dissipation term (curve 3) includes both friction and hyperviscosity. For relatively small vortices they have roughly equal order. The overall balance in the stationary linear-drag case is negative (for strong vortices) as dissipation tendency prevails,  $\mathcal{F} - \mathcal{D} + \mathcal{T} \leq 0$ . So strong vortices would decay unless sustained by mergers.

In the absence of friction or in the hypofrictional case, only hyperviscous dissipation acts on the vortex scale. Its contribution is overall smaller than the vorticity production by the source and this imbalance leads to the vortex growth.

The hypofriction case is intermediate between the linear drag and no-friction cases. Total energy slowly stabilizes at the equilibrium value, so numeric integration becomes less prohibitive. Figure 6(b) shows typical vortex tendencies for a hypofriction experiment (2h), at the equilibrium state. Vortex intensity (curve 1) grows slowly, mergers become more frequent but once again they may not lead to the net increase of intensity. In our example, it increases after the first merger but decreases after the second one. The forcing tendency (curve 2) is the strongest, while dissipation (curve 3) looks relatively shallow. Similar trends are observed for strong vortices in all hypofriction experiments.

Since hypofriction is negligibly small on the vortex scale, the dissipation comes entirely from the hyperviscosity [comparing dissipation tendencies of Figs. 6(b) and 6(a) one should keep in mind longer time interval and higher intensity

in 6(b). Mergers show up in the  $\mathcal{D}$  trend as sharp steps. Indeed, a merger would produce significant straining near vortex core and hence a burst of filamentation and rapid dissipation.

The residual term gives mostly negative contribution to the vortex growth between mergers contrary to the linear-drag trend.

Comparing two cases of Fig. 6 we could draw the following conclusions

(1) Forcing tendency  $\mathcal{F}(t)$  gives a consistent positive trend in all cases. Indeed, in the linear-drag case as well as in the early stage of hypofriction and no-friction regimes,  $\mathcal{F}(t)$  is the principal source of the vortex growth, while mergers play secondary role.

(2) The exact mechanism of the “vortex pump” needs further study. It should involve the rapid adjustment of vortex shape (2-rms contour) to the source tendency, as we found the core motion to remain relatively slow for strong vortices.

(3) Dissipation  $\mathcal{D}(t)$  gives consistent negative input but its relative value varies from case to case and depends on the vortex state.

(4) Residual (transfer) term  $\mathcal{T}(t)$  gives indeterminate input to a single realization and behaves differently in different regimes. In the hypofriction case its overall input is negative, except for large but rare merger events.

(5) In most cases the vortex fate would ultimately depend on the balance between  $\mathcal{F}$  and  $\mathcal{D}$ . Linear drag dampens equally all scales and could arrest vortex growth at a moderate level. Hypofriction does not affect small (horizontal) size and tips the balance over to the  $\mathcal{F}$  term, hence allowing strong vortices.

(6) Vortex growth would be arrested at some level because as vortices grow in size, the forcing tendency (per unit area) goes down. We observed this tendency for different vortex sizes and regimes but our data is insufficient to quantify it.

To understand the vortex growth mechanism D. Gurarie has developed a simple model of randomly forced radial vortex profiles (Gaussian, Rankine, etc.). They exhibit the basic phenomena of source accumulation, but more work is needed to verify the premises and conclusions of such model and compare it to numeric simulations.

### 3. Statistical growth dynamics

Finally we turn to statistical trends of vortex arrays, made of a few strongest vortices, or larger vortex populations. We based this study on experiments 15 and 2h with forcing wave number  $k_f=80$ , and exploited several regimes of vortex tracking and census.

In experiment 15 we took a stationary (developed) vorticity field and integrated it forward in time. A typical realization contains more than 500 vortices of mean level above  $2.4|\zeta_{rms}|$ . We took the first 200 of them, and followed their evolution over the friction time  $t=1/\lambda$ . Most vortices died out during that period and Fig. 7(a) shows their life span against their initial intensity.

The survival rate depends statistically on the vortex strength and the highest bin exhibits the highest rate. But a

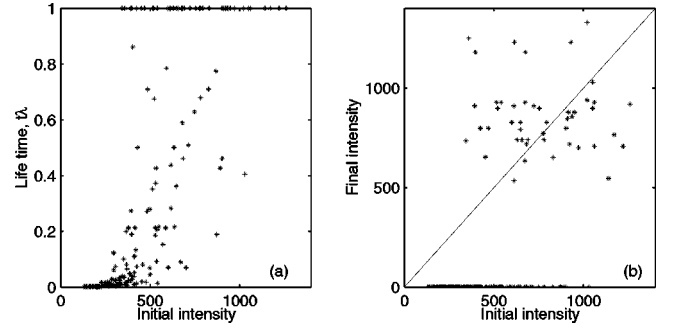


FIG. 7. Lifetimes of 200 vortices (a) and dependence of their final intensity (in  $t=1/\lambda$ ) on the initial intensity (b) in experiment 15.

fair number of moderately strong or weak vortices survived too as they gained strength in the process. Figure 7(b) plots the vortex terminal intensity against the initial one for that same group. We see a systematic transition pattern for the vortex population above 500-level: the strongest ones would go down to lower bins, while lower bins have tendency to move up or die out.

Thus, strong vortices are long-lived and persist on time scales comparable to  $1/\lambda$ . Their maximal intensity, however remains limited during the observation period. Overall the life span of even the strongest vortices is finite, so a typical evolution could take a vortex up to the high bin and then gradually bring it down. The offshoot of such stochastic growth-decay process is the stationary vortex distribution by intensity.

The detailed analysis of such stochastic (transition) process, its stationary ensemble, and its relation to the basic forcing-dissipation parameters poses a challenging problem.

Next we continued experiment 15 by tracking 10 strongest positive vortices. We used the vorticity field of 15 to initialize two other experiments: hypofriction (2h) and no friction (not listed in the table) to determine the effect of dissipation on the statistical growth process. Figure 8 shows long time series of 10 strongest vortices in experiment 15 (a), compared to the frictionless case (b). While the linear-drag case gives zero mean trend, the “no-friction” trajectories grow almost linearly in time.

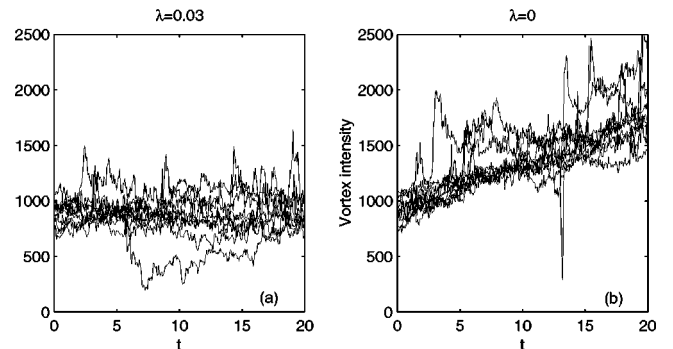


FIG. 8. Intensities of 10 strongest vortices vs time in experiment 15 (a) and in a similar experiment with  $\lambda=0$  (b). Initial vorticity field is the same in both cases.

A comparison of the two demonstrates the role of the linear drag in stabilizing the mean vortex intensity. Indeed, we estimate the growth tendency in Fig. 8(b) as 500 units per time  $1/(2\lambda)=16.7$ . Taking a simple growth model of the “mean-field” intensity,

$$\frac{d}{dt}I = \alpha - \lambda I, \quad (10)$$

with the growth tendency  $\alpha$  of Fig. 8(b), we find its stationary solution  $I = \alpha/\lambda \approx 1000$ , which comes close to the “mean level” of Fig. 8(a).

The (scale-dependent) hypofriction would still set a balance for the vortex growth (at a higher level), but we can’t write a simple “mean-field” model like Eq. (10) now. One would rather need a full “vortex spectrum” model with the stochastic “growth term” and scale-dependent dissipation to understand the hypofrictional turbulence in the energy range.

## V. DISCUSSION AND CONCLUSIONS

(1) Nonuniversal features of the forced 2D turbulence include departure from the  $k^{-5/3}$  spectra (at low  $k$ ), non-Gaussianity, and nonlocal irregular transfers. Those were traditionally viewed as artifacts of imperfect resolution or scale limitations imposed by finite size/geometry. We consider them more fundamental as any attempt to reproduce one feature (e.g., constant flux via small  $\lambda$  or hypofriction [8,12]) distorts the other (large deviations from  $k^{-5/3}$ ).

(2) Universal spectra seem to be exceptional and unstable to the formation of secondary structures, like strong vortices [10,8].

(3) The physical space reveals different levels of vorticity organization: (i) microscale (background), made of small patches and filaments sustained by forcing dissipation, and unstable to secondary structures; (ii) large-scale transient clusters, circulation zones, and jets; (iii) localized vortices (above  $2\xi_{rms}$ ).

(4) The background evolves rapidly from the rest state in the process of enstrophy saturation, while secondary structures grow through a slow process of energy saturation.

(5) Vortices appear in all regimes but local dynamics confines their size:  $(2-3)L_f$  in our experiments and up to  $5L_f$  in [8]. Under favorable conditions (no friction or hypofriction with sufficient enstrophy resolution) vortices could grow

strong (10–15 rms vorticity) and dominate the energy spectrum. They contribute to spectral bulge and steep spectral slope up to  $-3$ .

(6) The primary vortex growth mechanism is their ability to integrate source balanced in the long run by dissipation and to a lesser degree by nonlinear processes.

(7) Vortex mergers, typical of the decaying turbulence, seem to play little role in the forced case. They become more frequent, as vortices grow in size (and intensity), e.g., during slow hypofriction equilibration. But even then the forcing tendency dominates.

(8) The forcing trend  $\mathcal{F}$  (per unit area) decreases with the growth of vortex size. So eventually, nonlinear processes (like mergers) could take over, but we have not reached this stage. Besides,  $\mathcal{F}$  seems to be the only way to inject vorticity in the core, as other processes (mergers, etc.) could not raise its level.

(9) Dissipation term includes (hyper) viscosity and linear drag or hypofriction. The linear drag limits the vortex size and intensity, but hypofriction has little effect at the forcing scale and leads to slow growth of strong but slender vortices observed by Borue [8].

(10) One could view the physical space turbulence as a multiscale (in space time) stochastic process of the vortex growth decay on the background of “near Gaussian  $-5/3$  vorticity field,” whose transition probabilities could be linked to the basic parameters of forcing dissipation. We examined a few statistical features and trends, but further work is needed to develop this approach.

(11) The physical space view leaves many open problems like (i) “vortex-pump” mechanism: the ability to accumulate vorticity directly from stochastic source; (ii) the role of small (enstrophy) scales in vortex generation and growth, (iii) mechanism of frictional equilibration of the inverse cascade, given the absence of any structures, or processes on the energy-peak scale; and (iv) stochastic model of vortex growth dynamics in physical space, as counterpart to the standard “cascade phenomenology.”

## ACKNOWLEDGMENTS

This work was supported by the GTP program at NCAR. S.D. had additional support from NRC COBASE grant and RFBR Projects Nos. 99-05-64350 and 99-05-64351. We acknowledge helpful discussions with J. Herring.

- 
- [1] U. Frisch and P. L. Sulem, *Phys. Fluids* **8**, 1921 (1984).
  - [2] J. Herring and J. McWilliams, *J. Fluid Mech.* **153**, 229 (1985).
  - [3] L. M. Smith and V. Yakhot, *J. Fluid Mech.* **274**, 115 (1994).
  - [4] A. Babiano, B. Dubrulle, and P. Frick, *Phys. Rev. E* **52**, 3719 (1995).
  - [5] A. Babiano, B. Dubrulle, and P. Frick, *Phys. Rev. E* **55**, 2693 (1997).
  - [6] J. Paret and P. Tabeling, *Phys. Fluids* **10**, 3126 (1998).
  - [7] G. Boffetta, A. Celani, and M. Vergassola, *Phys. Rev. E* **61**, R29 (2000).
  - [8] V. Borue, *Phys. Rev. Lett.* **72**, 1475 (1994).
  - [9] M. E. Maltrud and G. K. Vallis, *Phys. Fluids* **A5**, 1760 (1993).
  - [10] M. E. Maltrud and G. K. Vallis, *J. Fluid Mech.* **228**, 321 (1991).
  - [11] A. Chekhlov, S. A. Orszag, S. Sukoriansky, B. Galperin, and I. Staroselsky, *Physica D* **98**, 321 (1996).
  - [12] S. Sukoriansky, B. Galperin, and A. Chekhlov, *Phys. Fluids* **11**, 3034 (1999).
  - [13] S. Danilov and D. Gurarie, *Phys. Rev. E* (to be published).
  - [14] G. S. Patterson and S. A. Orszag, *Phys. Fluids* **14**, 2538 (1971).
  - [15] D. R. Durran, *Mon. Weather Rev.* **119**, 702 (1991).

- [16] D. K. Lilly, *Geophys. Fluid Dyn.* **3**, 289 (1972).
- [17] J. C. McWilliams, *J. Fluid Mech.* **146**, 21 (1984).
- [18] R. Benzi, S. Patarnello, and P. Santangelo, *J. Phys. A* **21**, 1221 (1988).
- [19] J. C. McWilliams, *J. Fluid Mech.* **219**, 361 (1990).
- [20] A. Okubo, *Deep-Sea Res. Oceanogr. Abstr.* **17**, 445 (1970).
- [21] J. Weiss, *Physica D* **48**, 273 (1991).
- [22] D. Elhmaildi, A. Provenzale, and A. Babiano, *J. Fluid Mech.* **257**, 533 (1994).
- [23] B. L. Hua and P. Klein, *Physica D* **113**, 98 (1998).
- [24] O. G. Oetzel and G. K. Vallis, *Phys. Fluids* **9**, 2991 (1997).
- [25] G. F. Carnevale, J. C. McWilliams, Y. Pomeau, J. B. Weiss, and W. R. Young, *Phys. Rev. Lett.* **66**, 2735 (1991).